The Microscale Obstacle Resolving Meteorological Model MITRAS: Model Theory

Mohamed H. Salim[1,2*], K. Heinke Schlünzen[1†], David Grawe[1,†], Marita Boettcher[1], Andrea M. U. Gierisch[1,3], and Björn H. Fock[1,4]

[1]Meteorological Institute, CEN, University of Hamburg, Germany.
[2]Now: Faculty of Energy Engineering, Aswan University, Egypt.
[3]Now: Finnish Meteorological Institute, Marine Research, Helsinki, Finland.
[4]Now: Met Office, United Kingdom.
†Contact for the model: metras@uni-hamburg.de

Correspondence to: Mohamed Hefny Salim (mohamed.salim@uni-hamburg.de)

Abstract. This paper describes the developing theory and the underlying processes of the microscale obstacle resolving model MITRAS Version 2. MITRAS calculates wind, temperature, humidity and precipitation fields as well as transport within the obstacles layer using Reynolds averaging. It explicitly resolves obstacles, including buildings and overhanging obstacles, to consider their aerodynamic and thermodynamic effects. Buildings are represented by impermeable grid cells at the building positions so that the wind speed vanishes and zero turbulent kinetic energy is assumed in these grid cells. Wall functions are used to calculate appropriate turbulent fluxes. Most exchange processes at the obstacle surfaces are considered in MITRAS, including convective and radiative processes in order to obtain an accurate surface temperature. MITRAS is also able to simulate the effect of wind turbines. They are parameterized using the actuator-disk concept to account for the reduction in wind speed. The turbulence generation in the wake of a wind turbine is parameterized by adding an additional part to the turbulence mechanical production term in the turbulent kinetic energy equation. Effects of trees are considered explicitly, including the wind speed reduction, turbulence production, and dissipation due to drag forces from plant foliage elements as well as the radiation absorption and shading. The paper is providing not only a documentation of the model dynamics and numerical framework but also a solid foundation for future microscale model extensions.

1 Introduction

The urban boundary layer is considerably influenced by its surface characteristics. Within the canopy layer, the atmospheric flow is disturbed by buildings and other obstacles located at the surface, and hence all related atmospheric processes (Meng 2015). This creates a complex three-dimensional, time dependent flow, temperature and humidity field. Studying the atmospheric boundary layer flow and its interactions with complex terrain in e.g. urban areas is a complex problem for both the meteorological and engineering communities. Field experiments are one approach (e.g. Schafer et al. (2005)), however, field measurements have a low spatial representativeness and largely depend on the turbulence structure within the urban area and the wind direction fluctuations. This implies that long averaging times are needed in order to obtain reasonable time-

averaged-values; on the other hand long averaging times are not feasible because the atmospheric situation changes due to, e.g. the diurnal cycle or synoptic changes. Also, investigating future scenarios is not possible from field measurements. Subsequently, laboratory experiments in controlled conditions (wind tunnel) are used to overcome these problems after matching the major similarity parameters with the full scale model. These physical models can be very detailed (Harms et al.

5   2011) and can provide comparison data for numerical models and field experiments (VDI 2015). However, wind tunnel modeling is mostly limited to neutral atmospheric stratification due to the requirement to fulfill the similarity to nature. Furthermore, it is sometimes difficult to satisfy the atmospheric boundary conditions and to resemble important features of the Earth system such as Coriolis force effect. Alternatively, high-resolution numerical computer models are frequently used to simulate urban areas.

10   Numerical modeling of wind flow and pollutant dispersion in urban areas is a challenging task due to the geometrical variety of buildings. It inevitably involves impingement and separation regions, a multiple vortex system with building wakes, and jet effects in street canyons (Murakami et al. 1999). Furthermore, the neighbor buildings add their own impacts on the urban meteorology resulting in interacting flow and dispersion patterns. Due to this complexity, explicit resolving of the buildings is necessary instead of only implicitly considering building effects by using surface roughness parameterizations. This gave the

15   rise to the development of obstacle resolving microscale meteorological models such as ASMUS (Gross 2012), ENVI-met (Bruse and Fleer 1998; Müller et al. 2014), MISKAM (Eichhorn 1989; Eichhorn and Kniffka 2010), MUKLIMO (Früh et al. 2011), MITRAS (Schlünzen et al. 2003; Salim et al. 2011) or OpenFOAM (Franke et al. 2012). These models are now widely used for environmental and engineering studies.

The microscale obstacle resolving transport and stream model MITRAS is specific since it is part of the M-SYS model system

20   (Trukenmuller et al. 2004; Schatzmann et al. 2006). This model system is designed to investigate pollution transport, chemical reactions and atmospheric phenomena in the atmospheric boundary layer. The obstacle resolving MITRAS model calculates wind, temperature, humidity fields, cloud and rain water as well as tracer transport within the obstacle layer. The model has been applied for more than 10 years, however, an overall description of the model theory has not been published in a refereed journal. It is timely now, since the computers now allow for time dependent long-term integration of the temperature and

25   humidity equations in high resolution. In addition, MITRAS in its version 2 was extended and optimized for more realistic applications in urban areas (Salim et al. 2011; Röber et al. 2013). Specifically, more surface cover classes were added to better describe the surface characteristics: fine tuning the code structure for maximum parallelization to make it faster and able to simulate larger domains, and parameterizing the additional radiation, turbulence production and dissipation due to wind turbines and urban vegetation.

30   Model validations of MITRAS-01 have been performed in comparison to wind tunnel data (Schlünzen et al. 2003; Grawe et al. 2013). MITRAS 2 is evaluated using the VDI guideline for obstacle resolving microscale models (Grawe 2015). The results will be presented in a separate paper.

Equations and solution method will be described in Chapter 2, including the turbulence parameterization (Section 2.2) and numerical treatment (Section 2.3). Further sub-grid scale processes need to be parameterized, even in a very high resolving

atmospheric model like MITRAS. This concerns cloud microphysical processes and radiation. Both are calculated with the same parameterizations as its sister model METRAS (Schlünzen 1990; Schlünzen et al. 2011). The boundary conditions, including surface, lateral and top boundaries, are given in Chapter 3. The treatment of obstacle induced effects is described in Chapter 4, including wind, shading and heat transfer effects. MITRAS parameterizes momentum and heat fluxes on obstacle

5 surfaces dependent on the local roughness length (Sections 4.1, 4.2) and explicitly resolves obstacles, such as buildings including overhanging obstacles (e.g. bridges or overpasses), trees and wind turbines, to account for its aerodynamics and thermodynamic effects. The handling of wind turbines in the model and their effects is described in Section 4.3. Vegetation effects and especially their effect on radiation are given in Section 4.4.

2 Model Theory

10 ### 2.1 Model equations

MITRAS is based on the physical conservation equations, specifically, the Navier–Stokes equations, the continuity equation and the conservation equation for scalar quantities such as potential temperature and humidity. This set of equations is written in flux form, transformed in a terrain following coordinate system and filtered before it is used in MITRAS.

2.1.1 Coordinate transformation

15 The equations of MITRAS in flux form are transformed in a 3-dimensional non-uniform terrain-following coordinate system $\dot{x}^1, \dot{x}^2, \dot{x}^3$ so that the lower boundary conforms to the terrain. The vertical coordinate is defined by

$$\dot{x}^3 = z_t \frac{z - z_s(x,y)}{z_t - z_s(x,y)} \tag{1}$$

Here $z_s(x,y)$ is the orography height and z_t is the domain height. The terrain following coordinates ensure an easy specification of the boundary conditions over orography and eases nesting of MITRAS in METRAS due to the use of the same vertical coordinate transformation. The used transformation allows a grid stretching in all three directions to keep a high resolution in

20 the focus area of the domain while allowing some distance between the open boundaries (lateral and top) and the area of interest. In addition, the coordinate system can be rotated against North in any desired angle allowing for additional flexibility. Figure 1 shows an example of a vertical cross-section in this terrain-following coordinate system.

2.1.2 Filtering of equations, basic state and approximations

The filtering of the equation is applied after the coordinate transformation to ensure all possible fluctuations are included with

25 their correct contravariant and covariant components. The atmospheric state variables are divided into a value $\bar{\psi}$ which is the average over a finite time, $\Delta\tau$, and grid volume, $\Delta x \cdot \Delta y \cdot \Delta z$ and its deviation ψ' (Pielke 2002). The deviations are assumed to be zero if averaged over $\Delta\tau$ (classical Reynolds averaging approach). The average $\bar{\psi}$ is further decomposed for temperature,

humidity, concentration, pressure and density into a large scale part ψ_0, the so named basic state, and a microscale deviation $\tilde{\psi}$. The basic state is intentionally chosen to be steady state and fulfilling basic concepts of meteorology. For example the base state pressure p0 is chosen so that it satisfies the hydrostatic approximation and the vertical gradient is thus balancing $g\rho_0$. This ensures a higher order of accuracy when solving the equations, especially for the vertical wind. ψ_o represents a domain

5 average value using the values in the same height above sea level:

$$\psi_o = \frac{1}{\delta x \, \delta y} \int_{y_a}^{y_a+\delta y} \int_{x_a}^{x_a+\delta x} \overline{\psi} \, dx \, dy \tag{2}$$

y_a and x_a are the coordinate of a corner of the model and $\delta x \, \delta y$ the domain size in x- and y direction.

To increase the numerical accuracy further, the pressure deviation $\tilde{p}$ is decomposed into a quasi-hydrostatic pressure p_1 (in balance with $g\tilde{\rho}$) and a more or less dynamically impacted part p_2, where $p_2 = \tilde{p} - p_1$. Both ρ' and p' are neglected assuming $\rho' \ll \tilde{\rho}$ and $p' \ll \tilde{p}$. The Boussinesq approximation is used, thus density variations in the Navier-Stokes equations are

10 neglected except for the buoyancy term. P_2 is determined from an elliptic differential equation, which is derived from the anelastic approximation of the continuity equation, resulting in a decoupling of pressure and density in the model and hence no sound waves propagation. In addition to the above equations, the ideal gas law and the equation for the potential temperature are solved diagnostically.

2.1.3 Solved equations

15 The solved prognostic equations in MITRAS are as follows

$$\frac{\partial \rho_0 \alpha^* \overline{u}}{\partial t} = -\frac{\partial}{\partial \dot{x}^1}\left(\overline{u}\frac{\partial \dot{x}^1}{\partial x}\rho_0 \alpha^* \overline{u}\right) - \frac{\partial}{\partial \dot{x}^2}\left(\overline{v}\frac{\partial \dot{x}^2}{\partial y}\rho_0 \alpha^* \overline{u}\right) - \frac{\partial}{\partial \dot{x}^3}\left(\overline{\dot{u}}^3 \rho_0 \alpha^* \overline{u}\right)$$
$$- \alpha^* \frac{\partial \dot{x}^1}{\partial x}\left(\frac{\partial p_1}{\partial \dot{x}^1} + \frac{\partial p_2}{\partial \dot{x}^1}\right) - \alpha^* \frac{\partial \dot{x}^3}{\partial x}\frac{\partial p_2}{\partial \dot{x}^3} + \tilde{\rho}\alpha^* g \frac{\partial \dot{x}^3}{\partial x}\frac{\partial z}{\partial \dot{x}^3} + f\rho_0 \alpha^*\left(\overline{v} - V_g\right) \tag{3}$$
$$- f'd'\rho_0 \alpha^* \overline{w} - \overline{F}_1$$

$$\frac{\partial \rho_0 \alpha^* \overline{v}}{\partial t} = -\frac{\partial}{\partial \dot{x}^1}\left(\overline{u}\frac{\partial \dot{x}^1}{\partial x}\rho_0 \alpha^* \overline{v}\right) - \frac{\partial}{\partial \dot{x}^2}\left(\overline{v}\frac{\partial \dot{x}^2}{\partial y}\rho_0 \alpha^* \overline{v}\right) - \frac{\partial}{\partial \dot{x}^3}\left(\overline{\dot{u}}^3 \rho_0 \alpha^* \overline{v}\right)$$
$$- \alpha^* \frac{\partial \dot{x}^2}{\partial y}\left(\frac{\partial p_1}{\partial \dot{x}^2} + \frac{\partial p_2}{\partial \dot{x}^2}\right) - \alpha^* \frac{\partial \dot{x}^3}{\partial y}\frac{\partial p_2}{\partial \dot{x}^3} + \tilde{\rho}\alpha^* g \frac{\partial \dot{x}^3}{\partial y}\frac{\partial z}{\partial \dot{x}^3} - f\rho_0 \alpha^*\left(\overline{u} - U_g\right) \tag{4}$$
$$+ f'd\rho_0 \alpha^* \overline{w} - \overline{F}_2$$

$$\frac{\partial \rho_0 \alpha^* \overline{w}}{\partial t} = -\frac{\partial}{\partial \dot{x}^1}\left(\overline{u}\frac{\partial \dot{x}^1}{\partial x}\rho_0 \alpha^* \overline{w}\right) - \frac{\partial}{\partial \dot{x}^2}\left(\overline{v}\frac{\partial \dot{x}^2}{\partial y}\rho_0 \alpha^* \overline{w}\right) - \frac{\partial}{\partial \dot{x}^3}\left(\overline{\dot{u}}^3 \rho_0 \alpha^* \overline{w}\right) - \alpha^* \frac{\partial \dot{x}^3}{\partial z}\frac{\partial p_2}{\partial \dot{x}^3}$$
$$+ f' \rho_0 \alpha^* (\overline{u}d' - \overline{v}d) - \overline{F}_3 \tag{5}$$

$$\frac{\partial \rho_0 \alpha^* \overline{\chi}}{\partial t} = -\frac{\partial}{\partial \dot{x}^1}\left(\overline{u}\frac{\partial \dot{x}^1}{\partial x}\rho_0 \alpha^* \overline{\chi}\right) - \frac{\partial}{\partial \dot{x}^2}\left(\overline{v}\frac{\partial \dot{x}^2}{\partial y}\rho_0 \alpha^* \overline{\chi}\right) - \frac{\partial}{\partial \dot{x}^3}\left(\overline{\dot{u}}^3 \rho_0 \alpha^* \overline{\chi}\right) + \rho_0 \alpha^* \overline{Q}_{\overline{\chi}} - \overline{F}_{\overline{\chi}} \tag{6}$$

$\overline{u}, \overline{v},$ and $\overline{w}$ are the wind velocity components in the Cartesian coordinates, $\overline{\dot{u}}^3$ is the contravariant vertical component of the wind vector, α^* denotes a grid volume, $(\dot{x}^1, \dot{x}^2, \dot{x}^3)$ and (x, y, z) are the coordinates of the terrain following coordinate system and in the Cartesian system, respectively. The Coriolis parameters f and $\acute{f}$ are calculated according to the local geographic

5 latitude φ and the angular velocity of the Earth's rotation Ω as $f = 2\,\Omega\sin\,\varphi$ and $\acute{f} = 2\,\Omega\cos\,\varphi$. The variables $d = \sin\xi$ and $d' = \cos\xi$ account for the rotation of the coordinate system by an angle ξ against North. The terms $\overline{F}_1, \overline{F}_2, \overline{F}_2$ and $\overline{F}_\chi$ are the subgrid scale (SGS) turbulent momentum and scalar fluxes emerging from filtering the equations.

2.2 Parameterization of turbulent fluxes

2.2.1 Closure for momentum fluxes

10 Due to the filtering subgrid scale (SGS) fluxes arise. The three SGS turbulent fluxes in the momentum equations ($j = 1, 2, 3$) are:

$$\overline{F}_j = \frac{\partial}{\partial \dot{x}^1}\left(\rho_0 \alpha^* \overline{u'u'_j}\frac{\partial \dot{x}^1}{\partial x}\right) + \frac{\partial}{\partial \dot{x}^2}\left(\rho_0 \alpha^* \overline{v'u'_j}\frac{\partial \dot{x}^2}{\partial y}\right)$$
$$+ \frac{\partial}{\partial \dot{x}^3}\rho_0 \alpha^*\left(\overline{u'u'_j}\frac{\partial \dot{x}^3}{\partial x} + \overline{v'u'_j}\frac{\partial \dot{x}^3}{\partial y} + \overline{w'u'_j}\frac{\partial \dot{x}^3}{\partial z}\right) \tag{7}$$

The SGS fluxes can be expressed in terms of the Reynolds stress tensor τ_{ij}, which is related to the deformation tensor through the turbulent mixing coefficient (*Lilly* 1962; *Smagorinsky* 1963).

At the lowest model layer, the validity of Monin-Obukov surface layer similarity theory (*Monin and*

15 *Obukhov* 1954; *Foken* 2006) is assumed. The grid box averaged values of u_*, θ_*, q_{v*} are calculated using stability functions of Dyer (1974) with von Karman constant $\kappa = 0.4$.

Above the lowermost model layer the SGS turbulent fluxes are derived from a first order closure (*Detering* 1985; *Etling* 1987),

$$\tau_{ij} = -\rho_O \overline{u_i' u_j'} = \rho_O K_{ij} \left(\frac{\partial \overline{u_i}}{\partial \dot{x}^k} \frac{\partial \dot{x}^k}{\partial x_j} + \frac{\partial \overline{u_j}}{\partial \dot{x}^k} \frac{\partial \dot{x}^k}{\partial x_i} \right) - \frac{2}{3} \rho_O \delta_{ij} E \tag{8}$$

K_{ij} is the turbulent exchange coefficient for momentum in the x_j-direction. The last term in Eq. (8) represents the reduction of the diagonal fluxes due to pressure. Since this term is small compared to the deformation tensor term, it is neglected in MITRAS. Due to the symmetry of τ_{ij}, the actually calculated exchange coefficients are only a horizontal exchange coefficient (K_{hor}) and a vertical exchange coefficient (K_{vert}).

2.2.2 Closure for fluxes of scalar quantities

The turbulent fluxes for scalar quantities, e.g. potential temperature, are expressed as:

$$\bar{F}_\chi = \frac{\partial}{\partial \dot{x}^1} \left(\rho_0 \alpha^* \overline{u'\chi} \frac{\partial \dot{x}^1}{\partial x} \right) + \frac{\partial}{\partial \dot{x}^2} \left(\rho_0 \alpha^* \overline{v'\chi} \frac{\partial \dot{x}^2}{\partial y} \right) + \frac{\partial}{\partial \dot{x}^3} \rho_0 \alpha^* \left(\overline{u'\chi} \frac{\partial \dot{x}^3}{\partial x} + \overline{v'\chi} \frac{\partial \dot{x}^3}{\partial y} + \overline{w'\chi} \frac{\partial \dot{x}^3}{\partial z} \right) \tag{9}$$

These fluxes are also parameterized by a first order closure,

$$-\rho_O \overline{u_i' \chi'} = \rho_O K_{i\chi} \left(\frac{\partial \overline{\chi}}{\partial \dot{x}^k} \frac{\partial \dot{x}^k}{\partial x_j} \right) \tag{10}$$

$K_{i\chi}$ is the corresponding mixing coefficient in the x_i-direction, which is related to K_{ij}.

The exchange coefficients in MITRAS are either calculated using the Prandtl-Kolmogorov-closure (Section 2.2.2.1) or the E-ε turbulence closure (Section 2.2.2.2). In both turbulence closures the exchange coefficients are calculated as a function of the SGS turbulent kinetic energy E, for which an additional prognostic equation similar to Eq. (6) is solved. For the E-ε turbulence closure the dissipation εis additionally calculated from a prognostic equation (*López, et al.* 2005).

2.2.2.1 Prandtl-Kolmogorov-closure

The exchange coefficients are calculated as follows,

$$K_{vert} = c_1 l \bar{E}^{1/2} f(Ri) \tag{11}$$

c_1 is a free constant determined by matching the theoretical model against experimental values. It has the value 0.55 in MITRAS (*López* 2002). The Richardson number *Ri* dependent term is defined as

$$f(Ri) = \begin{cases} 1 - 5Ri & \text{for } Ri > 0 \\ (1 - 16Ri)^{1/4} & \text{for } Ri \leq 0 \end{cases} \tag{12}$$

and in accordance with the stability functions used in the surface layer. For the SGS turbulent kinetic energy, E, a prognostic equation is solved. The dissipation rate ϵ is calculated diagnostically as:

$$\epsilon = c_\epsilon \frac{\overline{E}^{3/2}}{l} \tag{13}$$

c_ϵ is a constant set to 0.166 (*López* 2002). The local mixing length l is related to the stability function ϕ_m and the distance to the nearest solid surface z_w, which can be the ground surface or a surface of a resolved obstacle. The equation of l reads:

$$l = \frac{\kappa z_w}{1 + \kappa \frac{z_w}{\lambda}} \phi_m \tag{14}$$

5   λ is the maximum eddy size (a value of 100 m is used).

2.2.2.2 *E-ε* turbulence closure

This closure is based on the standard *E-ε* model and the *Kato* and *Launder* (1993) modifications which eliminate the excessive turbulent kinetic energy production produced by the standard *E-ε* model in stagnation regions (*López et al.* 2005). The mechanical production term P_M in the *E*-equation can be derived according to the *Kato* and *Launder* (1993) modifications as

$$P_M = c_\mu \epsilon S \Omega \tag{15}$$

10   S is the dimensionless strain rate:

$$S = \frac{E}{\varepsilon} \sqrt{\frac{1}{2} \left(\frac{\partial \overline{u_i}}{\partial x_j} + \frac{\partial \overline{u_j}}{\partial x_i} \right)^2} \tag{16}$$

Ω is the rotation rate:

$$\Omega = \frac{E}{\varepsilon} \sqrt{\frac{1}{2} \left(\frac{\partial \overline{u_i}}{\partial x_j} - \frac{\partial \overline{u_j}}{\partial x_i} \right)^2} \tag{17}$$

which goes to zero near the stagnation point and so P_M is significantly reduced.

It has been shown by *Schlünzen et al.* (2003) that using *Kato* and *Launder* (1993) modifications for both the turbulent kinetic energy equation and the dissipation equation in MITRAS leads to overestimation of the momentum fluxes at stagnation point.

15   To overcome this drawback, they suggested limiting the *Kato* and *Launder* reformulation to the energy equation only. So, for the ε-equation, the P_M term is calculated the same way as in the standard *E-ε* model

$$P_M = c_\mu \epsilon S^2 \tag{18}$$

The buoyancy term is calculated in the same way as in the Prandtl-Kolmogorov-closure. The values for the constants c_1, c_2, c_μ are taken as suggested by López (2005) as $c_\mu = 0.09$, $c_1 = 1.44$, $c_2 = 1.92$.

2.3 Numerical solution

2.3.1 Discretization

5 The model equations are solved using finite volume methods on a staggered Arakawa C-grid (*Arakawa* and *Lamb* 1977). On this grid, scalar variables are defined at the cell center while the velocity components are defined on their respective normal cell faces (Figure 2). The obstacles faces are set where the corresponding wall normal velocity components are defined. Since u, v, w, and the scalar variables are defined at different locations in space, four index arrays are needed to describe the obstacle in the discretized 3D model domain. The discretization allows grid stretching in both vertical and horizontal directions to keep

10 focus on the inner part in the domain. The scalar points are always in the center of a grid cell, while the wind components might have different distances to the next-neighbor scalar grid point.

2.3.2 Numerical scheme

The advection and diffusion terms in the momentum equations are solved in MITRAS using the Adam-Bashforth scheme in time and centered differences in space. The vertical diffusion terms are determined using the Crank Nicholson implicit scheme

15 in order to increase the time step for vertical exchange processes. All other terms in the momentum equations except dynamic pressure p_2 are solved forward in time and centered in space.

The dynamic pressure p_2 is determined iteratively from a Poisson equation to satisfy the anelastic approximation. MITRAS allows two user-selected options for the iterative procedures, the iterative IGCG-scheme (Idealized Generalized Conjugate Gradient; (*Kapitza* and *Eppel* 1987)) and the preconditioned BiCGStab-method (BiConjugate Gradient Stabilized; (*Van der*

20 *Vorst* 1992)).

To avoid numerical artifacts which might appear due to non-linear interactions and result in short-wave energy accumulation, the value of diffusivity is increased by adding diffusivity.

Advection of scalar quantities is solved forward in time and using the upstream scheme for advection. Even so the upstream method is known for being diffusive with its implicit diffusivity K_{num} in e.g. x-direction given by $K_{num} = 0.5 \cdot |U| \cdot \Delta x \cdot$

25 $(1 - Co)$ (*Roache* 1982), the artificial diffusivity is acceptable in the target area of the domain for two reasons: a) the isotropic grid and building impacts ensures advection and diffusion in horizontal and vertical direction being of comparable size and b) advection is often larger than diffusion terms since the SGS turbulence is small within the canopy layer. U is the local wind speed, Δx is the local grid width, and Co is the Courant number.

Since Eqs. (13) and (14) imply that dissipation rate and subgrid scale turbulent kinetic energy are directly coupled, the

30 dissipation cannot be calculated with very large time steps. Eq. (13) is solved by determining an analytic solution (Appendix A) as suggested by *Fock* (2015). This avoids unphysical values of ϵ, which might even be negative for large time steps Δt.

3 Boundary Conditions

In MITRAS, several types of boundary conditions can be used in physically consistent combinations to allow for different kinds of simulations. At the ground surface (lower boundary) and obstacle faces (Section 4) material interfaces are given, while the lateral boundaries and the upper boundary are artificial due to the use of a limited area model.

3.1 Surface boundary

a. Wind velocity

For the horizontal wind velocity components, a no-slip boundary condition ($\bar{u}_j = 0$, j=1, 2) is used at all vertical surfaces. With this the vertical wind defined in the staggered grid at the surface, results to zero too. Since u and v are defined at the lowest level at k=0.5 (Figure 2) on the staggered grid, a Neumann boundary condition is used with a constant gradient using the zero surface values. By this the no-slip condition is achieved at the surface. Additional details for buildings are given in Section 4.1.

b. Dynamic pressure (p_2)

The boundary condition for the pressure p_2 is formulated by considering the wind velocity boundary condition, the grid staggering, the position of the domain boundaries and the dynamic pressure equation. Consistent with the no-slip boundary condition the boundary condition used for p_2 at the wall is:

$$\frac{\partial \dot{x}^1}{\partial x}\frac{\partial \dot{x}^3}{\partial x}\frac{\partial p_2}{\partial \dot{x}^1} + \frac{\partial \dot{x}^2}{\partial y}\frac{\partial \dot{x}^3}{\partial y}\frac{\partial p_2}{\partial \dot{x}^2} + \left(\left(\frac{\partial \dot{x}^3}{\partial x}\right)^2 + \left(\frac{\partial \dot{x}^3}{\partial y}\right)^2 + \left(\frac{\partial \dot{x}^3}{\partial z}\right)^2\right)\frac{\partial p_2}{\partial \dot{x}^3} = 0 \qquad (19)$$

Due to the terrain following coordinate system (Eq. 1) the vertical gradient of the dynamic pressure p_2 needs to be zero perpendicular to the surface.

c. Temperature

The calculated temperature values of all physical boundaries (ground and obstacles surfaces, i.e. wall and roof) are used at the lower boundary and at the obstacle surfaces. The necessary additions for buildings are provided in Section 4.2. These temperature values are calculated based on the energy balance using the surface energy budget equation

$$R_{SW,net} + R_{LW,net} + Q_S + Q_L + Q_G + Q_A = 0 \qquad (20)$$

$R_{SW,net}$ and $R_{LW,net}$ are the net shortwave and longwave radiation fluxes, Q_S is the sensible heat flux, Q_L is the latent heat flux, Q_G is the ground heat flux, and Q_A is the anthropogenic heat emission flux.

Both $R_{SW,net}$ and $R_{LW,net}$ are calculated using the atmospheric radiation scheme of MITRAS's sister model METRAS (Schlünzen et al. 2011) and the surface characteristics, i.e. the albedo value. Influence of vegetation as well as the shading from the obstacles is taken into account in the calculation of radiation (Section 4.4). The fluxes Q_S and Q_L are calculated with respect to the thermal stratification using the friction velocity u_* and the scaling values for heat, θ_*, and water vapor, q_*.

The heat flux from the ground to the surface is calculated by:

$$Q_G = \nu_s \left(\frac{\partial T}{\partial z}\right)_s \tag{21}$$

ν_s is the thermal conductivity. Following Tiedtke and Geleyn (1975) and Deardorff (1978) equations the force-restore method is used for the ground soil heat flux:

$$\frac{\partial T_s}{\partial t} = \frac{2\sqrt{\pi}\kappa_s}{\nu_s h_\theta}\left(H - \sqrt{\pi}\nu_s \frac{T - T(-h_\theta)}{h_\theta}\right) \tag{22}$$

T_s is the temperature at the surface, H is the force term including all fluxes in Eq. (20) except Q_G, $T(-h_\theta)$ is the deep soil
5 temperature, h_θ represents the depth of the daily temperature wave in the restore term and κ_s is the thermal diffusivity of the surface cover material.

For obstacles, the calculated surface temperature (Section 4.2) of the obstacle surfaces is used at the corresponding grid cells.

d. Humidity

The following budget equation, introduced by Deardorff (1978), is used to calculate the humidity at the lower boundary ($\bar{q}_{1s}$):

$$\bar{q}_{1s} = \alpha_q \bar{q}_{1\text{sat}}(\bar{T}_s) + (1 - \alpha_q)\bar{q}_1 \tag{23}$$

10 α_q is the soil water availability and $\bar{q}_{1\text{sat}}(\bar{T}_s)$ is the saturated humidity at $\bar{T}_s$. The initial value of α_q is given for each surface cover class (Section 0). A prognostic equation is used to calculate α_q in the time dependent model integration:

$$\frac{\partial \alpha_q}{\partial t} = \frac{Q_E/l + P}{\rho_w W_k} \tag{24}$$

Q_E is the turbulent humidity flux at the surface (calculated in consistency with Q_L), $l = 2.5 \cdot 10^6$ J kg^{-1} is the latent heat of vaporization of water, P is the precipitation (if any), ρ_w water density, and W_k is the saturation value for water content. This is prescribed for each surface cover class (Section 0).

15 *e. Other scalar quantities*

At the ground surface and at the obstacle surface E and ϵ are calculated as a function of local friction velocity, as follow:

$$E_{z=0} = \frac{u_*^2}{c_1^2}, \quad \epsilon_{z=0} = \frac{u_*^3}{\kappa z_0}. \tag{25}$$

The empirical constant c_1 is set to the same value as in Eq. (11). This helps together with Eq. (12) to get continuous fluxes at the top of the lowest model cell, which employs the surface layer scheme (Lopez 2002, Fock 2015).

3.2 Lateral

20 *a. Wind velocity*

Dirichlet boundary conditions are used in two different formulations. They can be used in MITRAS in arbitrary combinations to describe the lateral boundaries of the domain: open boundary (radiative) and fixed boundaries. The appropriate combination of boundary value calculations depends on the application. For instance, a realistic application, with comparison to field data in mind, needs open boundaries. In these the boundary normal wind components are calculated as far as possible from the

5   prognostic equations. The boundary normal advection is treated by the use of the Orlanski condition at inflow boundaries and by the upstream scheme at outflow boundaries. For the boundary parallel velocity components a zero-flux condition is assumed (Schlünzen 1990).

When comparison with wind tunnel measurements (e.g. Grawe et al. (2014)) is performed, fixed boundaries are advantageous. In these the wind profiles are to be imposed at the inlet boundary and kept fixed at the initial values while at the outflow the

10   wind velocity is treated as an open boundary.

b. Other variables

The normal gradients of pressure p_2, temperature, humidity and concentrations are set to zero at the lateral boundaries.

3.3 Top

a. Wind velocity

15   For the vertical wind, which is defined at the model top, Dirichlet condition is used, prescribing it to initial values (mostly vertical wind zero). For all other variables a Neumann boundary condition is employed, where the gradients normal to the boundary are zero. In order to avoid reflections of vertically propagating waves at the upper model boundary, Rayleigh damping layers (absorbing layers) are used in MITRAS. The Rayleigh damping terms, which are added to the flow equations (Eqs. 3-6), are written here following *Clark* (1977) and *Durran* and *Klemp* (1982)

$$R_1 = -\rho_0 \alpha^* (\overline{u} - U_g) v_R \tag{26}$$

$$R_2 = -\rho_0 \alpha^* (\overline{v} - V_g) v_R \tag{27}$$

$$R_3 = -\rho_0 \alpha^* \overline{w} v_R \tag{28}$$

20   U_g and V_g are the geostrophic wind velocity components and v_R is the relaxation coefficient, defined as

$$v_R = \begin{cases} 0 & \text{for } k < k_D \\ \delta^{(k_t - k)} & \text{for } k \geq k_D \end{cases} \tag{29}$$

k denotes the vertical grid point index, k_t the index of the highest grid point at the upper boundary and k_D the index of the first absorbing layer.

b. Other variables

The normal pressure gradient, temperature gradient, turbulent momentum fluxes and their gradients are all set to zero at the

25   upper boundary. This assumption results in zero vertical heat and moisture fluxes as well as zero momentum fluxes at the upper model boundary.

4 Treatment of obstacles

4.1 Buildings

The concept of the mask method (*Briscolini* and *Santangelo* 1989) is employed in MITRAS to explicitly resolve the buildings within the 3-D model domain. This method is based on the immersed boundary method (*Mittal* and *Iaccarino* 2005) which

5   allows flow simulation in the vicinity of complex geometries that do not conform on Cartesian grids. Impermeable grid cells at the buildings positions are defined using 3-D fields of weighting factors, *vol(x,y,z)*, defined at each grid cell to give information about whether a grid cell is an atmospheric cell or a building cell (which lies mostly or completely inside a building). Any faces of a grid volume that are a wall or roof of a building are marked. This means that the grid cells in a domain are divided into three groups: grid cells in the free atmosphere surrounded by atmosphere without any adjacent building, grid

10 cells next to building surfaces, and grid cells within buildings, as shown in Figure 3. This separation facilitates the model coding and economizes the computational requirements.

A building mask containing these data is prepared by the preprocessor GRIMASK (Section 5.3). In the model, e.g. the wind velocity components vanish at the building boundaries by multiplying the fluxes with the face markers (impermeable walls). Additional wall functions are included to properly address friction effects.

15 Building surfaces influence the ambient air temperature. Their effect is taken into account by simulating the sensible heat flux. In grid cells that are adjacent to building surfaces, the term Q_θ is added to the turbulent fluxes of heat (Eq. 9).

$$Q_\theta = -u_{b*}\theta_{b*} \tag{30}$$

represents the temperature flux, which is calculated from the friction velocity at buildings, $u_{b\theta}$, and the scaling value for potential temperature, θ_{b*}. $u_{b\theta}$ is calculated following the approach of *Lopez* (2002) as

$$u_{b*} = \kappa \frac{|\vec{v}_b|}{ln\left(\frac{d_b}{z_{b,0}}\right)} \tag{31}$$

assuming a logarithmic wind profile with neutral stratification over the building surface. $|\vec{v}_b|$ is the wind speed parallel to the

20 building surface at the first scalar grid cell next to the building surface, i.e. in the distance d_b. $z_{b,0}$ is the roughness length of the building surface. The scaling value for potential temperature at buildings is calculated as

$$\theta_{b*} = \kappa \frac{(\overline{\theta_{d,b}} - \theta_b)}{ln\left(\frac{d_b}{z_{b,0}}\right)} \tag{32}$$

from the difference of the building surface temperature, θ_b, and the temperature at the first grid cell next to the building, $\theta_{d,b}$. The roughness length for temperature at the building is

$$z_{b,0,\theta} = z_{b,0} . min\left(exp\left(7.3\kappa \sqrt[4]{\frac{u_* z_{b,0}}{\nu}} \sqrt{Pr} - 5 \right), 442413 \right) \tag{33}$$

with the kinematic viscosity ν and the Prandtl number Pr = 0:71.

This concept allows considering not only surface-mounted buildings but also overhanging obstacles such as bridges and overpasses. They can all be considered in complex urban geometries.

4.2 Building surface temperature

5   In order to obtain an accurate surface temperature of the buildings (obstacles), most exchange processes at the building surfaces are considered in MITRAS, including convective and radiative processes (*Gierisch* 2011). Thus, the physical properties of the façade and walls materials are to be introduced as model inputs. These properties include reflectivity, emissivity, heat transfer coefficient, and specific heat capacity.

The surface temperature of a building surface, T_b, is calculated from the energy budget of the infinitely thin outermost slab of

10   the building façade. The slab is heated or cooled from outside by a heat source H and supported from inside by the rest of the façade that is connected to the building interior. Latter is assumed to be maintained at the constant temperature T_{in}.

The rate of temperature change of the slab is governed by the imbalance between the forcing term H and a restoring term. The prognostic equation for the surface temperature reads

$$c_{wall} D \frac{\partial T_b}{\partial t} = H - \frac{\lambda}{D}(T_b - T_{in}). \tag{34}$$

Here the forcing term H is calculated from

$$H = R_{SW,abs} + R_{LW,abs} - \varepsilon\sigma T_b^4 + Q_S + Q_L. \tag{35}$$

15   $R_{SW,abs}$ and $R_{LW,abs}$ are the absorbed incoming short wave and long wave radiation, Q_S and Q_L are the sensible and latent heat fluxes at the surface which are calculated from the local friction velocity and the local scaling values for temperature and humidity (*Gierisch* 2011), λ is the thermal conductivity, D is the wall thickness, and c_{wall} is the wall volumetric heat capacity.

The surface energy balance for the inside wall surface can be written as

$$Q_C - h_i(T_{in} - T_{room}) = 0. \tag{36}$$

h_i is the heat transfer coefficient for the internal wall, and Q_C the heat conduction flux through the wall calculated as $Q_C =$

20   $\frac{\lambda}{D}(T_b - T_{in})$ and T_{room} is the room temperature.

From Eq.(36), the relation between T_{in} and T_b is

$$T_{in} = \frac{h_i}{h_i + \frac{\lambda}{D}} T_{room} + \frac{\frac{\lambda}{D}}{h_i + \frac{\lambda}{D}} T_b \tag{37}$$

Substituting for H and T_{in} in Eq.(34) yields,

$$\frac{\partial T_b}{\partial t} = \frac{1}{c_{wall} \, D} [H - C(T_b - T_{room})]. \tag{38}$$

The right-hand side of Eq. (38) is a function of T_b. Thus

$$\frac{\partial T_b}{\partial t} = F(T_b). \tag{39}$$

Applying the backward implicit scheme to Eq.(39),

$$F(T_b^{t+\Delta t}) = F(T_b^t) + \left. \frac{\partial F}{\partial T_b} \right|_{T_b^t} (T_b^{t+\Delta t} - T_b^t) \tag{40}$$

and solving for $T_b^{t+\Delta t}$ gives the time dependent equation for the surface temperature:

$$T_b^{t+\Delta t} = T_b^t + \frac{F(T_b^t)}{\frac{1}{\Delta t} - \left. \frac{\partial F}{\partial T_b} \right|_{T_b^t}} \tag{41}$$

4.3 Wind turbines

Wind turbines are represented in MITRAS by impermeable grid cells at the position of the tower and the nacelle, similar to other buildings (i.e. vanishing wind speed and zero turbulent kinetic energy are assumed at grid points within the tower and nacelle). The orientation of the nacelle changes in relation to the wind direction during the model simulation. The wind turbine rotor is parameterized by using the actuator-disk concept (*Molly* 1978; *Mikkelsen* 2003; *El Kasmi* and *Masson* 2008). In this concept the rotor is replaced by an imaginary permeable disk subjected to a distribution of forces which acts upon the incoming flow at a rate defined by the period-averaged kinetic energy that the rotor extracts from the atmosphere.

According to the actuator-disk model, the reduction of the wind speed is caused by the rotor thrust, *T*, which is formulated as.

$$T = \frac{1}{2} c_T \rho A V_1^2. \tag{42}$$

V_1 is the speed of the approaching flow at wind turbine level, *A* is the rotor area, ρ is the air density, and c_T is the non-dimensional thrust coefficient. The wind speed deficit is limited to those cells located at the actual rotor position. The speed of

the approaching flow is calculated with respect to the orientation of the rotor which depends on wind direction and changes direction during the simulation. The thrust coefficient depends on wind speed and therefore the wind turbine automatically switches on and off in MITRAS at the cut-in and cut-off wind speed, respectively.

This wind turbine rotor blades creates wake vortices of the wind turbines, which are associated with increased turbulence

5   intensity. The turbulence generation in the wake is parameterized in MITRAS by adding an additional term, Q_{wt}, to the turbulence mechanical production, P_M, in the turbulent kinetic energy equation to account for the turbulence generation at the rotor position. This term is formulated as:

$$Q_{wt} = \frac{1}{2} c_{wt} u_{wt}{}^2 \tag{43}$$

c_{wt} depends on the wind turbine rotational speed and its geometrical characteristics, such as the rotor size and the number of blades, and u_{wt} is a scale velocity used to characterize the turbulence.

10   In MITRAS, the tangential velocity v_θ, which is frequently used to model the vortex developing behind an aircraft, is used as the scale velocity. The Rankine vortex model (*Gerz et al.* 2001) is applied here to calculate v_θ

$$v_\theta = \frac{\Gamma_O}{2\pi r_c} \tag{44}$$

r_c is the vortex core radius and Γ_O is the rotor circulation, which is related to the rotor rotational speed, lift coefficient, and aspect ratio. More details about modeling the wind turbines in MITRAS are given in *Linde* (2011).

4.4 Vegetation

15   There are two modes of vegetation treatment in MITRAS: the implicit mode and the explicit mode. In the implicit mode, the effect of the vegetation (grass, bushes, trees, etc.) is implicitly considered in the surface parameterization, using the roughness length. This is done by allocating the vegetation surface cover class for the corresponding surface grid cells and using the corresponding input parameters (e.g. roughness length, soil water content etc.; Section 5.2).

In the explicit mode, the vegetation effects are explicitly resolved. These effects include the wind speed reduction (*Schlüter*

20   2006), turbulence dissipation due to drag forces from plant foliage-atmosphere interaction (*Salim et al.* 2015), and radiation absorption and shading.

The wind speed reduction is parameterized by introducing a local three-dimensional sink term, S_{u_i} with *i=1, 2, 3* for the u-, v, w- component. S_{u_i} is added to the momentum equations (3-5). Following *Liu* (1996), the sink term is calculated as:

$$S_{u_i} = - c_d \, LAD(\dot{x}^3) \cdot U \cdot u_i \tag{45}$$

Here c_d is a drag coefficient, U is the mean wind speed at height $\dot{x}^3$, and $LAD(\dot{x}^3)$ is the equivalent leaf area density of the

25   plant at height $\dot{x}^3$. The value of $c_d = 0.2$ determined by *Katul* (1998) is chosen here.

S_{u_i} represents a source of turbulence due to extraction of mean kinetic energy, E, from the flow. However, the typical effect of vegetation is to reduce the overall turbulence model by enhancing the dissipation of turbulence. To parameterize the additional turbulence creation and dissipation, additional source terms are added to the turbulent kinetic energy and dissipation equations. Following *Wilson* (1988) and *Liu et al.* (1996) these terms read:

$$Q_{veg,E} = c_d LAD(\dot{x}^3) \cdot U^3 - 4c_d LAD(\dot{x}^3) \cdot |U| \cdot E \tag{46}$$

$$Q_{veg,\epsilon} = 1.5c_d LAD(\dot{x}^3) \cdot U^3 - 6c_d LAD(\dot{x}^3) \cdot |U| \cdot \epsilon \tag{47}$$

5   The reduction of the shortwave radiation flux is considered by including local reduction coefficients (ranged from 1 to 0) according to the vegetation characteristics. The reduction coefficients are described in terms of the vertical leaf area index, LAI, of the plant (see Section 5.4)

$$\sigma_{SW}(\dot{x}^3) = \exp(F \cdot LAI(\dot{x}^3)) \tag{48}$$

5 Model Input

Several model inputs are required to run the model MITRAS to accurately simulate a domain for, e.g. an urban area (Figure
10   4). These include for instance the orography heights of the domain, the surface cover types, the building data (dimensions, shape, and position), and the vegetation data for such a domain. Integrating these inputs to the computational domain of MITRAS is done in a separate preprocessor called GRIMASK (*Salim*, 2014). A complete description of this pre-processor is outside the scope of this paper, but the required input data and how they are in general achieved is outlined here (Sections 5.1-5.4). Moreover, the representative meteorological conditions for the domain are required as inputs to run MITRAS; they are
15   provided in consistency with the model physics and numeric using a pre-processor.

5.1 Orography Height

Urban domains might include elevated terrain. To better describe the domain's terrain, the orographic effects of the domain are considered in MITRAS by virtue of the terrain-following coordinate system (Section 2.1). Both the aerodynamic as well as the radiative (shading) effects of the slopes are considered in MITRAS. For realistic applications, the orography data (terrain
20   height above sea level) of the domain are introduced to GRIMASK in a standard ASCII grid format of a geographic information system (GIS). Usually these data are in much finer resolution (less than 0.25 m) compared to the computational domain horizontal resolution (~ 1 m). GRIMASK then aggregates these data to the surface grid cells to calculate the average orography height for each surface grid cell. This is done by splitting down each grid cell into n sub-grids and calculating the orography height of each sub-grid. The eventual orography height, z_s, of a grid cell (i, j) is calculated from

$$z_s(i,j) = \frac{1}{n}\sum_{1}^{n} z_{sub}(x,y) \tag{49}$$

$z_{sub}(x,y)$ is the orography height of a sub-grid.

For idealized studies and test cases, GRIMASK can generate artificial orography heights according to the objective of the test case, e.g. a bell mouth hill or a Gaussian hill.

5.2 Surface Cover

5   It is essential to define the surface cover characteristics of the urban domain because they govern the surface energy budget (Eq. 19) and all surface dependent fluxes. In realistic cases, the urban domain usually contains several surface cover types (water, sealed surfaces, vegetation, sand, ice, etc.) and it becomes imperative to define an appropriate data structure to encode information on surface cover characteristics. To this purpose, the surface cover data are first introduced to GRIMASK in the GIS standard ASCII grid format. GRIMASK then integrates these data into the computational grid cells at the surface. Each

10   grid cell is composed of at least one surface cover class, but more SGS surface covers are allowed. The pre-processor calculates how many surface cover classes exist in the domain as well as the portion of each surface cover class in each grid cell. This is done following the approach used to calculate the orography heights. Each grid cell at the surface is divided into sub-grids and the surface cover class of each sub-grid is defined. The data structure of the surface cover consists of two data sets: a) the portion of each surface cover class in each grid cell and b) a list of surface cover classes existing in the domain. Several classes

15   are prepared in the surface cover class database also for the different vegetation types (coniferous trees, deciduous trees, bushes, etc.). A data-base of several surface cover classes with attributed physical parameters is available in the 1-D MITRAS model. The physical parameters given per surface cover class include albedo (A), roughness length (z_0), thermal diffusivity (K), thermal conductivity (ν), soil water availability (α_q), and saturation value for water content (W_k). The physical parameters are given in Table 1 for selected surface cover classes.

20   For buildings normally the explicit treatment is chosen. If the implicit consideration of obstacles is chosen, i.e. they are not explicitly resolved in the model grid, a much larger roughness length would be required which conflicts with a high vertical grid resolution. This is similarly true for trees. The roughness length for water is modified during the model calculations in dependence on wind speed (*Fischereit et al.* 2016). The roughness length of scalar quantities over water, z_{0a}, is calculated for $a=\theta$ with a value of 0.76 and for $a = q$ with a value of 0.6, dependent on the roughness length for momentum, z_0 (*Brutsaert*

25   1975; *Brutsaert* 2013):

$$\frac{z_0(x,y)}{z_{0a}(x,y)} = \max\left(z_0/442413, \exp\left(\kappa\left(7.3Re^{1/4}\sqrt{a} - 5\right)\right)\right) \tag{50}$$

Re is the Reynolds number.

To distinguish surface cover classes, water, buildings and sea ice identifiers are incorporated for each surface cover class. These act as the Kronecker delta function to mark the particular class. For instance, the water switch is defined as:

$$\delta_{j,water} = \begin{cases} 1, & if \ j \ \in 'water' \\ 0, & if \ j \ \notin 'water' \end{cases} \tag{51}$$

j is the surface cover class index.

5.3 Building data

In order to generate the building mask used to provide the building data to the model, detailed information about the buildings in the domain is required. For instance, the building dimensions, shape, and location are needed for each building located in the domain to calculate the 3-D array *vol* and the building wall based markers discussed in Section 0. This process is done in the preprocessor, GRIMASK, which allocates the buildings to the computational grid.

Since in the current version of MITRAS the 3-D field *vol* can be either 0 (building cell) or 1 (atmosphere cell), buildings are approximated to fit into the grid. For grid cells that are partially filled with buildings, the determination of whether these cells are building or atmosphere cells depends on how much volume of the cell is filled with building. A grid cell is considered a building cell if at least 50% of its volume contains building. Otherwise it is counted as an atmosphere cell. This approximation is computationally efficient to consider the effect of the buildings since the model equations only need to be multiplied by the 3-D field *vol*.

For realistic applications, the complex urban building geometry can be provided to GRIMASK in either the raster Digital Elevation Model (DEM) format, which is commonly used due to the advances in remote sensing technologies, or in the ASCII 3-D Computer-Aided Design (CAD) format. GRIMASK integrates the high resolution DEM data, which is a grid of squares representing the elevation of each small grid, to the computational grid and calculates how much volume of the building is contained in each grid cell. When the building data is provided in the ASCII CAD format, GRIMASK uses an approach similar to z-buffering to integrate the building surfaces (usually triangles) to the computational grid and calculates the array *vol* and the face markers.

5.4 Vegetation

The vegetation input to MITRAS depends on the selected vegetation treatment in the model. In the implicit mode, the vegetation is defined as a surface cover class (Section 5.2). In the explicit mode, however, the vegetation inputs are the 3-D arrays *LAD* and *LAI*, prepared by GRIMASK. Two approaches are available in GRIMASK in order to calculate these arrays based on the available plant data: the measurement approach and the analytic approach. In the first approach, the following data for each plant in the model area are processed in GRIMASK: the measured 1-D vertical leaf area index profile $LAI(\dot{x}^3)$, the plant height, and the plant location. The following relation is used to relate *LAD* and *LAI*:

$$LAI(\dot{x}^3 + \Delta z) = \int_z^{z+\Delta z} LAD(\dot{x}^3)dz \tag{52}$$

In the analytical approach, GRIMASK uses the following empirical relation proposed by *Lalic* and *Mihailovic* (2004) to describe LAD profile from plant parameters:

$$LAD(\dot{x}^3) = LAD_m \left(\frac{h - z_m}{h - \dot{x}^3}\right)^n \exp\left[n\left(1 - \frac{h - z_m}{h - \dot{x}^3}\right)\right] \quad (53)$$

LAD_m is the maximum LAD, h is the plant height above z_s, z_m is the corresponding height above z_s, and

$$n = \begin{cases} 6 & 0 \le \dot{x}^3 < z_m \\ \frac{1}{2} & z_m \le \dot{x}^3 < h \end{cases} \quad (54)$$

The plant parameters used in these equations can be obtained from the forest phenology calendar.

5.5 Meteorology

The large-scale surface friction free meteorological situation is required as input to the model MITRAS to calculate the microclimate of a certain domain. This input is prepared by a one-dimensional model without explicit consideration of buildings but with inclusion of all relevant turbulence processes (including surface friction and Coriolis force) to provide the required meteorology data needed for the initialization of all the variables in the three-dimensional model. Among the inputs for the one-dimensional model are: the large scale speed wind components which is taken to be the geostrophic wind and should not include any frictional effects or wind rotation with height that will both be imposed by the 1D model, the large scale potential temperature gradient or temperature profile, the large scale relative humidity profile, the deep soil temperature, and the number of days without precipitation (dry days) prior to the simulation. The one-dimensional model calculates besides the initial values, the wind inflow profile if fixed boundary values are used and the values at the top boundary. Since the one-dimensional model calculates the average mesoscale conditions, large scale phenomena can be integrated into the model by controlling the inlet boundary condition using the time-slice approach for nesting (*Schlünzen* 1990). For some applications (e.g. comparisons with wind tunnel data) it is essential to fix the inflow profiles as described in Section 3.2.

6 Examples of model applications

This section provides examples of some simulations recently performed using MITRAS. The intent is not to provide model validations or verifications, as these will be done in a separate paper with focus on this aspect, but rather to give the readers some impression about the model capacities and potential.

6.1 Comparison to wind tunnel measurements

MITRAS results have been frequently compared to measurements of physical models. For instance, Grawe et al. (2012) compared MITRAS results, based on an earlier model version, to quality ensured wind tunnel data for both idealised (flow

around quasi-2-dimentional beam, single cubic obstacle, and array of cubic obstacles) and realistic (1×1 km^2 urban domain around Göttinger Straße in Hannover, Germany) test cases using standard evaluation procedures (VDI, 2005). The model results show a very good agreement with the measurements of the wind tunnel. Also, the model results, based on the current version, have been compared to the wind tunnel measurements of Michelstadt test case (an idealized model of a Central-European city, which is publicly available in the CEDVAL-LES database: http://www.mi.uni-hamburg.de/cedval-les). This has been done during the model validation using an updated evaluation guideline for prognostic microscale wind field models (Grawe et al. 2015).

6.2 Wind flow field in a realistic urban domain

MITRAS has been used to simulate the wind flow field in the city centre of Hamburg in Germany. The selected domain has a size of 2×2 km^2 and represents a typical urban area with many features of urban complexity such as complex building geometries, different street configurations, and diverse surface covers (including water bodies, street pavements and open spaces). All available building data (shapes, dimensions, locations, etc.), orography heights, and the surface cover characteristics of the domain are utilized to generate the required input data for MITRAS. The meteorological conditions used in this simulation are set so that the wind speed is 3 m/s at 200 m above ground and the wind direction is 230°, which is a typical wind direction in Hamburg. The results are shown in Fig. 5 where wind speed as well as vertical wind are plotted at the pedestrian height vertical level. The results describe the effects of buildings on the flow field and show several flow features such as wind speed acceleration in open areas and deceleration within dense building configurations and updrafts and downdrafts around the buildings. Moreover, the figure shows that not only do buildings alter the wind flow field but additionally the orography and surface characteristics modify the wind.

6.3 The effect of urban vegetation on wind field

MITRAS simulations with different parameterizations of urban vegetation (especially trees) were recently performed by Salim et al. (2015) to study the effect of the inclusion of trees when simulating the wind flow in different urban complexities. This study showed a significant effect of trees on the wind field and thus highlights the importance of the explicit representation of urban trees in microscale simulations. The snapshot of an animation created from the simulations performed in this study is shown in Fig. 6 and displays the wind field when the trees are considered in the simulation together with the trees sizes and locations. More details about this study can be found in Salim et al. (2015).

6.4 Thermal effect of buildings

To show the thermal effect of a building on its surroundings, several simulations have been done using MITRAS. The building surface temperature is calculated as described in Sec. 4.2 to simulate a single high-rise building located in an urban area in Hamburg on the 1st February at 13:30 (Gierisch 2011). Figure 7 shows the thermal effect of such building by comparing the air temperature field with a reference case, in which the thermal energy flux from building façades is neglected.

6.5 The impact of wind turbines on atmospheric flow

The model MITRAS with the embedded wind turbine parameterizations (see Section 4.3) has been used to produce simulation data for model validations (Linde 2011). The selected case in this study was the Nibe wind-turbines in Nibe city in Denmark. This case is selected because there is a meteorological measurement dataset for these wind turbines (Taylor 1990). Figure 8 gives one example of the model results performed in this study. Comparisons of model results with the measurements showed a good agreement.

7 Summary and Outlook

The model theory of the obstacle resolving microscale meteorological model MITRAS Version-2 has been described in this paper. Detailed descriptions of the model equations and their formulations and approximations are presented. The sub-grid scale turbulence parameterization used in MITRAS is outlined showing the Prandtl-Kolmogorov-closure and the 1.5-order E-ε turbulence closure. Also, the detailed parameterizations of obstacles such as the wind turbines and vegetation (trees) are introduced. The different boundary conditions implemented in MITRAS as well as the model inputs are also outlined. The model dynamics and numerical framework of the model MITRAS are established to provide a solid foundation for future model extensions.

Verification experiments of MITRAS Version-02 to the simulation of urban areas with explicitly resolved obstacles (including buildings, wind turbines and trees) will be presented in a separate paper. A recent application of MITRAS Version-02 on vegetation effects in urban areas can be found in *Salim et al.* (2015).

Code availability

Currently the MITRAS source code is distributed upon request under the terms of a user agreement with the Mesoscale and Microscale Modelling (MeMi) working group at the Meteorological Institute, the University of Hamburg (https://www.mi.uni-hamburg.de/memi). A copy of the user agreement is available upon request. Due to current copyright restrictions users are requested to contact the corresponding authors to obtain access to the code free of charge for research purposes under a collaboration agreement.

Documentation for the M-SYS model system, in which MITRAS is included, is available online at https://www.mi.uni-hamburg.de/memi under "Numerical Models".

Acknowledgement

This research is supported through the Cluster of Excellence 'CliSAP' (EXC177) and the research project UrbMod funded by the state of Hamburg, Germany.

Appendix A: Implicit method for dissipation of TKE

The numerical method for calculating the dissipation term in the SGS TKE equation is based on splitting the SGS TKE prognostic equation into two parts. In the first part all processes except the dissipation are integrated within a time step Δt to get a preliminary value of TKE, $\hat{E}$. In the second part TKE at the end of the complete time step $\hat{E}^{n+1}$ is used to integrate the dissipation term

$$\frac{\partial \hat{E}^{n+1}}{\partial t} = -\epsilon \tag{A.1}$$

The dissipation is parameterized according to Eq. 13, which can be simplified as

$$\epsilon = C \frac{\bar{E}^{3/2}}{l(Ri)} \tag{A.2}$$

where C is a constant.

Overall, the following equation is solved in the second step

$$\frac{\partial \rho_0 \alpha^* \hat{E}^{n+1}}{\partial t} = -\rho_0 \alpha^* C \frac{\hat{E}^{3/2}}{l(Ri)} \tag{A.3}$$

By integrating Eq. A.3, assuming ρ_0, α^* and $l(Ri)$ to be constant within one time step, the analytic solution for the TKE dissipation is calculated as follow,

$$\int_{\hat{E}^{n+1}}^{\bar{E}^{n+1}} \left(\hat{E}^{n+1}\right)^{-3/2} d\hat{E}^{n+1} = -\frac{C}{l(Ri)} \int_t^{t+\Delta t} dt \tag{A.4}$$

$$\bar{E}^{n+1} = \hat{E}^{n+1} \left(\frac{(\rho_0 \alpha^* C)^2}{4 l(Ri)^2} \Delta t^2 \hat{E}^{n+1} + \frac{\rho_0 \alpha^* C^2}{4 l(Ri)} \Delta t \sqrt{\hat{E}^{n+1}} + 1 \right)^{-1} \tag{A.5}$$

A similar solution for the dissipation term in the TKE equation of the SGS model suggested by *Deardorff* (1980), suitable for large eddy simulation, is presented in *Fock* (2015).

References

Arakawa, A., and Vivian, R. L.: Computational Design of the Basic Dynamical Processes of the UCLA General Circulation Model, Methods in Computational Physics, 17, 173–265, 1977.

Briscolini, M., and Santangelo, P.: Development of the Mask Method for Incompressible Unsteady Flows, Journal of Computational Physics, 84 (1), 57–75, 1989.

Bruse, M. and Heribert F.: Simulating Surface–plant–air Interactions inside Urban Environments with a Three Dimensional Numerical Model, Environmental Modelling & Software, 13, 373–84, 1998.

Brutsaert, W.: The Roughness Length for Water Vapor Sensible Heat, and Other Scalars, Journal of the Atmospheric Sciences, 32 (10), 2028–31, 1975.

5 Brutsaert, W.: Evaporation into the Atmosphere: Theory, History and Applications, Vol. 1. Springer Science & Business Media, https://books.google.de/books?hl=en&lr=&id=GW5-BgAAQBAJ&oi=fnd&pg=PA1859&dq=Evaporation+into+the+atmosphere:+theory,+history,+and+applications&ots=Dd28Pd3BFA&sig=BrKh3bduErYcjDsu0hINrUdWLgQ, 2013.

Clark, T. L.: A Small-Scale Dynamic Model Using a Terrain-Following Coordinate Transformation, Journal of Computational

10 Physics, 24, 186–215, 1977.

Deardorff, J. W.: Efficient Prediction of Ground Surface Temperature and Moisture, with Inclusion of a Layer of Vegetation, Journal of Geophysical Research: Oceans (1978–2012), 83, 1889–1903, 1978.

Deardorff, J. W.: Stratocumulus-capped mixed layers derived from a three-dimensional model, Boundary-Layer Meteorology 18.4, 495-527, 1980.

15 Detering, H. W.: Mixing Length and Turbulent Diffusion Coefficient in Atmospheric Simulation models, Thesis, Technische Univ., Hanover, Germany, 1985.

Durran, D. R. and Joseph, B. K.: The Effects of Moisture on Trapped Mountain Lee Waves, Journal of Atmospheric Sciences, 39, 2490–2506, 1982.

Dyer, A. J.: A Review of Flux-Profile Relationships, Boundary-Layer Meteorology, 7 (3), 363–72, 1974.

20 Eichhorn, J.: Entwicklung Und Anwendung Eines Dreidimensionalen Mikroskaligen Stadtklima-Modells, PhD diss. 1989.

Eichhorn, J. and Anke, K.: The Numerical Flow Model MISKAM: State of Development and Evaluation of the Basic Version, Meteorologische Zeitschrift, 19 (1), 81–90, 2010.

El Kasmi, A. and Christian M.: An Extended K–ε Model for Turbulent Flow through Horizontal-Axis Wind Turbines, Journal of Wind Engineering and Industrial Aerodynamics, 96, 103–22, 2008.

25 Etling, D.: The Planetary Boundary Layer PBL, Landlot-Börnstein:" Meteorology", Group V 4, 151–88, 1987.

Fischereit, K. Heinke Schlünzen, Andrea M. U. Gierisch, David Grawe, Ronny Petrik (2015): Modelling tidal influence on sea breezes with models of different complexity. Meteorologische Zeitschrift, doi: 10.1127/metz/2016/0703

Fock, B. H.: RANS versus LES Models for Investigations of the Urban Climate, Thesis, University of Hamburg, Hamburg, Germany. http://ediss.sub.uni-hamburg.de/volltexte/2015/7171/, 2015.

30 Foken, T.: 50 Years of the Monin–Obukhov Similarity Theory, Boundary-Layer Meteorology, 119 (3), 431–47, 2006.

Franke, J., Sturm, M., and Kalmbach, C.: Validation of OpenFOAM 1.6. X with the German VDI Guideline for Obstacle Resolving Micro-Scale Models, Journal of Wind Engineering and Industrial Aerodynamics, 104, 350–59, 2012.

Früh, B., Becker, P., Deutschländer, T., Hessel, J.D., Kossmann, M., Mieskes, I., Namyslo, J., Roos, M., Sievers, U., Steigerwald, T. and Turau, H.: Estimation of climate-change impacts on the urban heat load using an urban climate model and regional climate projections, Journal of Applied Meteorology and Climatology, 50(1), 167-184, 2011.

Gerz, T., Holzaepfel, F., Darracq, D., de Bruin, A., Elsenaar, A., Speijker, L., Harris, M., Vaughan, M. and Woodfield, A.A.:

5   Aircraft Wake Vortices–a Position Paper, Wakenet position paper, the European Thematic Network on Wake Vortex Position Paper, 2001.

Gierisch, A.: Mikroskalige Modellierung Meteorologischer Und Anthropogener Einflüsse Auf Die Wärmeabgabe Eines Gebäudes, Master Thesis, University of Hamburg, Hamburg, Germany, 2011.

Grawe, David et al.: An Updated Evaluation Guideline for Prognostic Microscale Wind Field Models, presented at the ICUC9,

10   Toulouse France, July 2015.

Grawe, D., Schlünzen, K. H., and Pascheke, F.: Comparison of Results of an Obstacle Resolving Microscale Model with Wind Tunnel Data, Atmospheric Environment, 79, 495–509, 2013.

Gross, G.: Effects of Different Vegetation on Temperature in an Urban Building Environment. Micro-Scale Numerical Experiments, Meteorologische Zeitschrift, 21 (4), 399–412, 2012.

15   Harms, F., Leitl, B., Schatzmann, M., and Patnaik, G.: Validating LES-Based Flow and Dispersion Models, Journal of Wind Engineering and Industrial Aerodynamics, 99 (4), 289–95, . 2011.

Kapitza, H., and Eppel, D.: A 3-D Poisson Solver Based on Conjugate Gradients Compared to Standard Iterative Methods and Its Performance on Vector Computers, Journal of Computational Physics, 68 (2), 474–84, 1987.

Kato, M., and Launder, B. E.: The Modelling of Turbulent Flow around Stationary and Square Cylinders, Ninth Symposium

20   on Turbulent Shear Flows, 1993.

Katul, G.: An Investigation of Higher-Order Closure Models for a Forested Canopy, Boundary-Layer Meteorology, 89 (1), 47–74, 1998.

Lalic, B. and Mihailovic, D.T.: An Empirical Relation Describing Leaf-Area Density inside the Forest for Environmental Modeling, Journal of Applied Meteorology 43 (4), 641–45, 2004.

25   Lilly, D. K.: On the Numerical Simulation of Buoyant Convection, Tellus, 14, 148–72, 1962.

Linde, M.: Modellierung Des Einflusses von Windkraftanlagen Auf Das Umgebende Windfeld, Master Thesis, University of Hamburg, Hamburg, Germany, 2011.

Liu, J., Chen, J.M., Black, T.A. and Novak, M.D.: E-ε Modelling of Turbulent Air Flow Downwind of a Model Forest Edge, Boundary-Layer Meteorology, 77, 21–44, 1996.

30   López, S. D.: Numerische Modellierung Turbulenter Umströmungen von Gebäuden, Berichte zur Polar-und Meeresforschung (Reports on Polar and Marine Research) 418, 2002.

López, S. D., Lupkes, C., and Schlunzen, K. H.: The Effect of Different K-Closures on the Results of a Micro-Scale Model for the Flow in the Obstacle Layer, Meteorologische Zeitschrift, 14, 839–48, 2005.

Meng, C.: The integrated urban land model." Journal of Advances in Modeling Earth Systems, 7(2), 759-773, 2015.

Mikkelsen, R.: Actuator Disc Methods Applied to Wind Turbines, PhD Thesis, Technical University of Denmark, Copenhagen, Denmark, 2003.

Mittal, R. and Iaccarino, G.: Immersed Boundary Methods, Annu. Rev. Fluid Mech., 37, 239–61, 2005.

Molly, Jens-Peter: Windenergie in Theorie Und Praxis: Grundlagen Und Einsatz, Müller, 1978.

5 Monin, A. S. and Obukhov, A.: Basic Laws of Turbulent Mixing in the Surface Layer of the Atmosphere, Contrib. Geophys. Inst. Acad. Sci., USSR 151, 163–87, 1954.

Müller, N., Kuttler, w., and Barlag, A.: Counteracting Urban Climate Change: Adaptation Measures and Their Effect on Thermal Comfort, Theoretical and Applied Climatology, 115 (1-2), 243–57, 2014.

Murakami, S., Ooka, R., Mochida, A., Yoshida, S., and Kim, S.: CFD Analysis of Wind Climate from Human Scale to Urban
10 Scale, Journal of Wind Engineering and Industrial Aerodynamics, 81, 57–81, 1999.

Pielke, R. A.: Mesoscale Meteorological Modeling, Academic press, 2002.

Roache, P. J.: Scaling of High-Reynolds-Number Weakly Separated Channel Flows, In Numerical and Physical Aspects of Aerodynamic Flows, 87–98, 1982. Springer. http://link.springer.com/chapter/10.1007/978-3-662-12610-3_6.

Röber, N. , Salim, M. H., Gierisch, A., Böttinger, M., and Schlünzen, K. H.: Visualization of Urban Micro-Climate
15 Simulations, The Eurographics Association, 53–57, 2013.

Salim, M. H., Schlünzen, K. H., and Grawe, D.: Including Trees in the Numerical Simulations of the Wind Flow in Urban Areas: Should We Care?, Journal of Wind Engineering and Industrial Aerodynamics, 144, 84–95, 2015.

Salim, M. H., Linde, M., Gierisch, A., and Schlünzen, K. H.: Some Recent Extensions and Applications of the Micro-Scale Model MITRAS, presented at the 10th European Conference on Applications of Meteorology (ECAM) / 11th EMS Annual
20 Meeting, Berlin, Germany, 2011.

Schafer, K., Emeis, S., Hoffmann, H., Jahn, C., Muller, W., Heits, B., Haase, D., Drunkenmolle, W.D., Bachlin, W., Schlunzen, K. and Leitl, B.: Field Measurements within a Quarter of a City Including a Street Canyon to Produce a Validation Data Set, International Journal of Environment and Pollution, 25 (1-4), 201–16, 2005.

Schatzmann, M., Bächlin, W., Emeis, S., Kühlwein, J., Leitl, B., Müller, W.J., Schäfer, K. and Schlünzen, H.: Development
25 and Validation of Tools for the Implementation of European Air Quality Policy in Germany (Project VALIUM), Atmospheric Chemistry and Physics, 6 (10), 3077–83, 2006.

Schlünzen, K. H.: Numerical Studies on the Inland Penetration of Sea Breeze Fronts at a Coastline with Tidally Flooded Mudflats, Contributions to Atmospheric Physics, 63 (3-4), 243–56, 1990.

Schlünzen, K. H., Flagg, D. D., Fock, B. H. Gierisch, A., Lüpkes, C., Reinhardt, V., and Spensberger, C.: Scientific
30 Documentation of the Multiscale Model System M-SYS (METRAS, MITRAS, MECTM, MICTM, MESIM, MEMI), Technical Report 4, Meteorologisches Institut KlimaCampus Universitaet Hamburg, 140 P., 2012. https://www.mi.uni-hamburg.de/en/arbeitsgruppen/memi/modelle/dokumentation/msys-scientific-documentation.pdf

Schlünzen, K.H., Hinneburg, D., Knoth, O., Lambrecht, M., Leitl, B., Lopez, S., Lüpkes, C., Panskus, H., Renner, E., Schatzmann, M. and Schoenemeyer, T.: Flow and Transport in the Obstacle Layer: First Results of the Micro-Scale Model MITRAS, Journal of Atmospheric Chemistry, 44, 113–30, 2003.

Schlüter, I.: Simulation Des Transports Biogener Emissionen in Und über Einem Waldbestand Mit Einem Mikroskaligen

5   Modellsystem, Master Thesis, University of Hamburg, Hamburg, Germany, 2006.

Smagorinsky, J.: General Circulation Experiments with The Primitive Equations: I. The Basic Experiment, Monthly Weather Review, 91, 99–164, 1963.

Taylor, G. J.: Wake measurements on the Nibe wind turbines in Denmark. Contractor report ETSU WN 5020, National Power - Technology and Environment Center, 1990.

10   Tiedtke, M. and Geleyn, J. F.: The DWD General Circulation Model- Description of Its Main Features, Beitraege Zur Physik Der Atmosphaere, 48, 255–77, 1975.

Trukenmuller, A., Grawe,G., and Schlunzen, K. H.: A Model System for the Assessment of Ambient Air Quality Conforming to EC Directives, Meteorologische Zeitschrift, 13, 387–94, 2004.

Van der Vorst, Henk A.: Bi-CGSTAB: A Fast and Smoothly Converging Variant of Bi-CG for the Solution of Nonsymmetric

15   Linear Systems, SIAM Journal on Scientific and Statistical Computing, 13 (2), 631–44, 1992.

VDI: Environmental Meteorology, Prognostic Microscale Wind Field Models, Evaluation for Flow around Buildings and Obstacles, VDI-Standard: VDI 3783 Blatt 9, 2015 http://www.vdi.eu/guidelines/vdi_3783_blatt_9-umweltmeteorologie_prognostische_mikroskalige_windfeldmodelle_evaluierung_fuer_gebaeude_und/

Wilson, J. D. 1988. "A Second-Order Closure Model for Flow through Vegetation." Boundary-Layer Meteorology 42: 371–

20   92.

VDI: Environmental Meteorology - Prognostic Microscale Wind Field Models - Evaluation for Flow Around Buildings and Obstacles. Technical Report, 2005. VDI Guideline 3783, Part 9. Commission on Air Pollution Prevention of VDI and DIN.
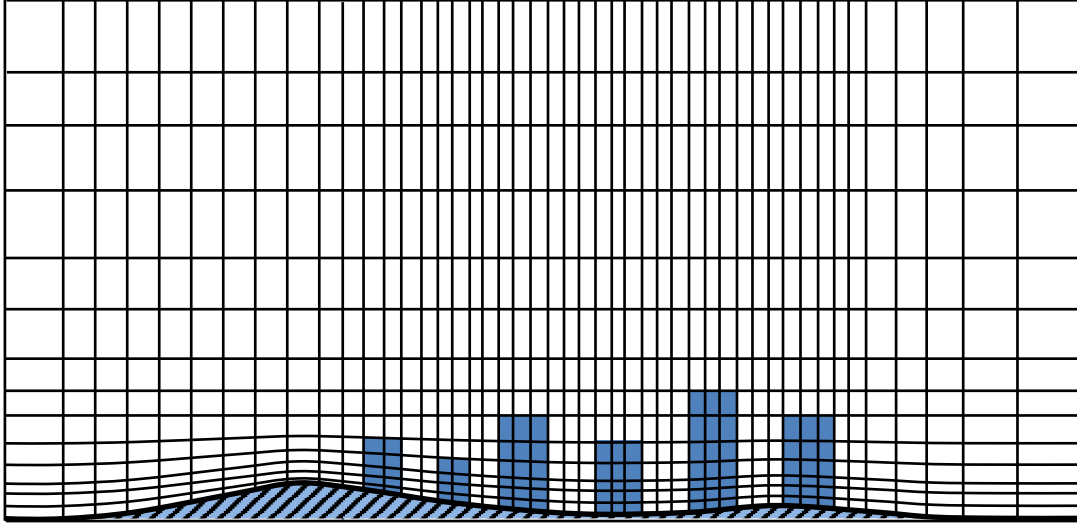
Figure 1: Vertical cross-section to illustrate the MITRAS grid in the terrain-following coordinate system. The blue blocks denote buildings. Not all grid cells are shown.
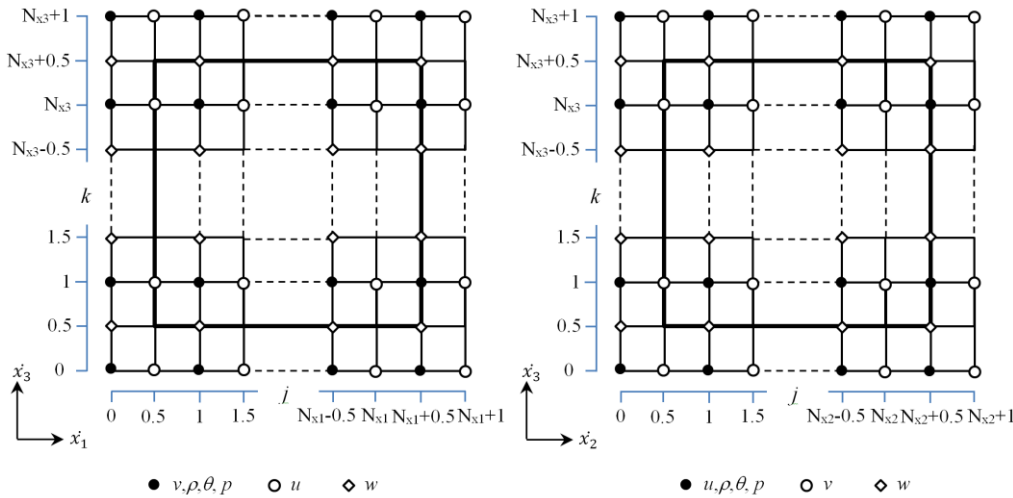
Figure 2: Sketch showing the staggering of the variables of a domain in (a) x-z-direction and (b) y-z-direction for a model domain with size of $N_{x1} \times N_{x2} \times N_{x3}$. The thick line denotes the model domain boundaries. For simplification a uniform grid is shown.
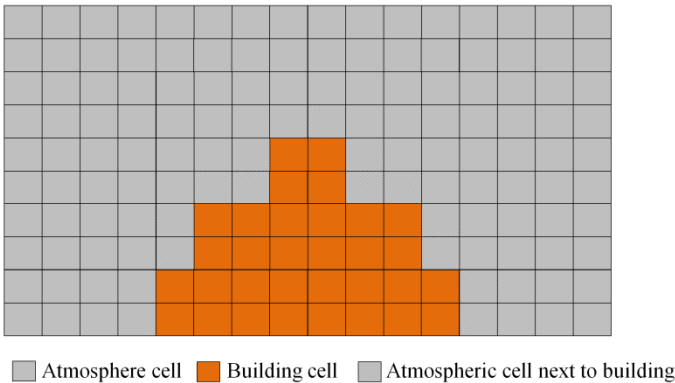
Figure 3: Masking concept in MITRAS
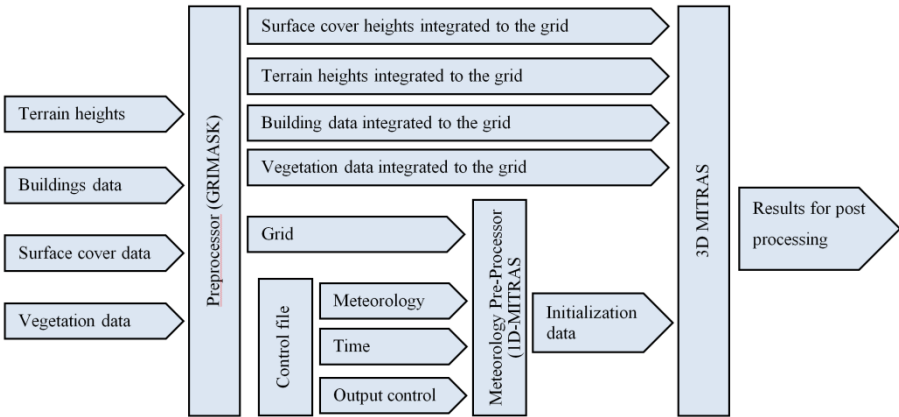
Figure 4: Principal elements of the MITRAS model inputs.
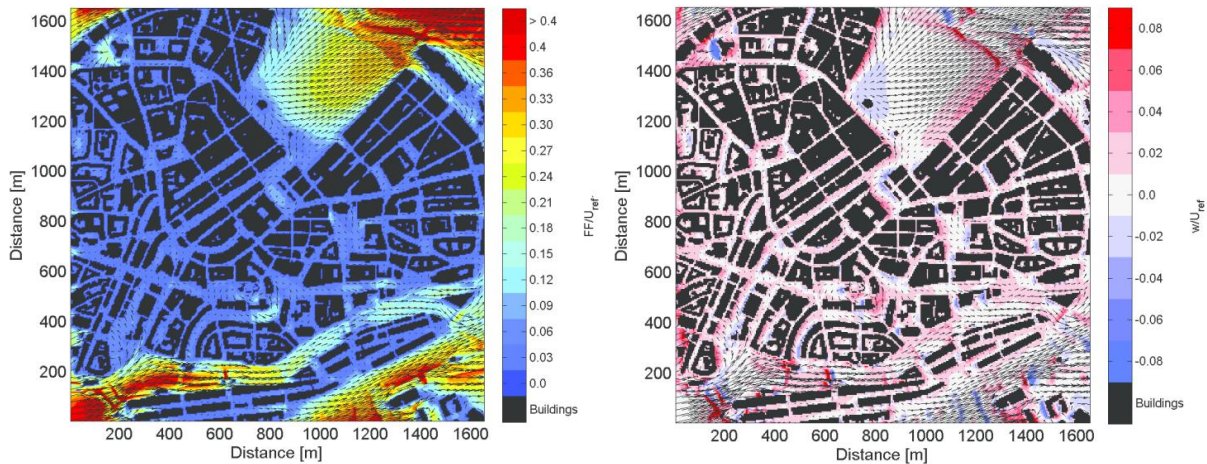
Figure 5: Wind field at pedestrian height level in the city centre of Hamburg (Germany) showing the normalized wind speed (left) and the vertical wind (right). The simulated domain size is approximately 2,000m × 2,000m where x- and y- axes are aligned to West-East and North-South directions, respectively. Simulated mean wind direction is South-West and the atmospheric stratification is neutral. A grid spacing of 5m in all spatial directions is used. All input data are taken from: Digital Terrain Model, the data of the Germangeo-information system ATKIS (Official Topographic-Cartographic Information System), and the 3D-urban model data (LoD2) for building details.
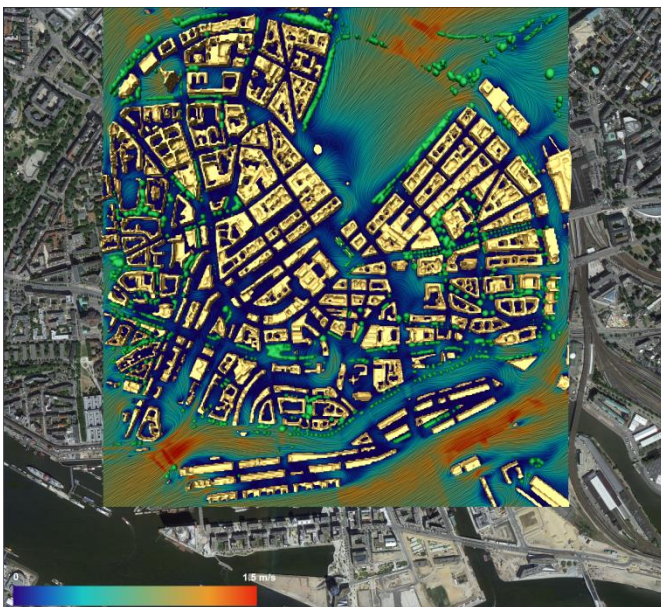
Figure 6: Snapshot of the wind speed in the city-centre of Hamburg (Germany) from a simulation which includes the effect of trees. The simulated domain (2000m × 2000m) contains about 2800 trees with 130 different species. Buildings as well as trees are displayed in shades of yellow and green, respectively. The animation setup was kindly provided by N. Röber at DKRZ. The copyright for the underlying satellite image is held by GeoBasis-DE/BKG (©2009), Google
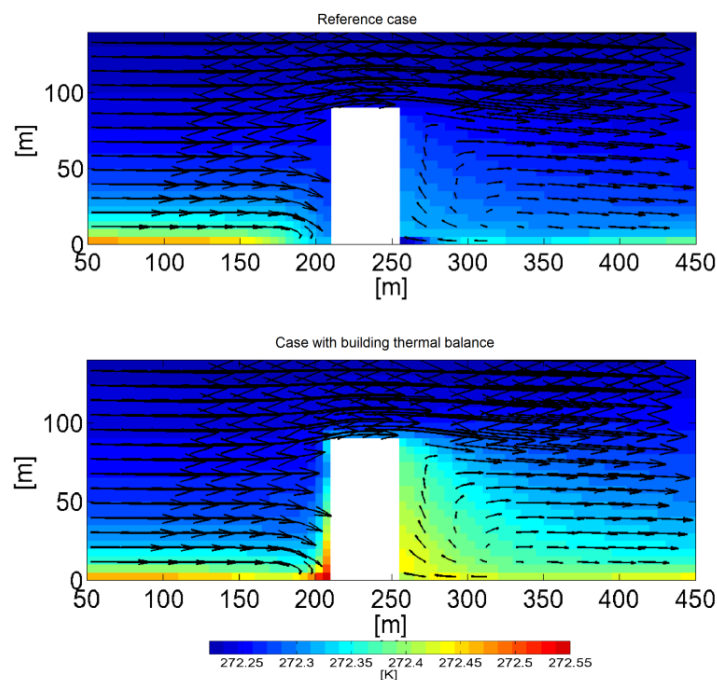
Figure 7: Vertical cross-section at the centre of a high-rise building located in Hamburg (Germany) on the 1st February at 13:30 parallel to the wind direction. Colors show the potential temperature of the air surrounding the building and arrows depict the wind circulation for both the reference case (no thermal energy exchange between building façades and environment, top panel) and the case with full model physics as described in Sec 4.2 (lower panel). Comparing both cases indicates that the air is slightly heated up by the buildings especially in the building stagnation and wake regions.
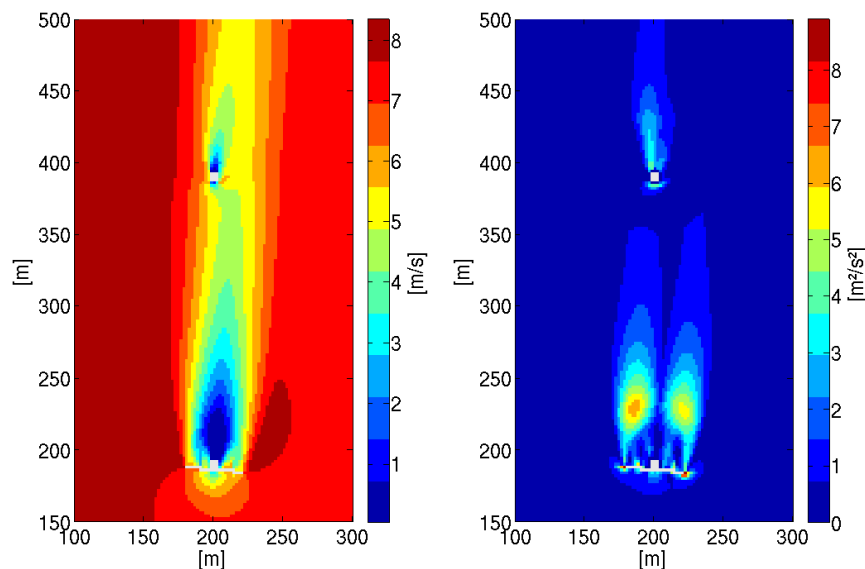
Figure 8: Horizontal cross-section of the domain at 38m high showing the wind speed (left) and the turbulent kinetic energy (right) in the vicinity of a wind turbine (Nibe B) and the tower of another wind turbine (Nibe A, out of service in the simulation). A mean wind flow of 8.5 m/s speed and South direction was simulated in a neutrally stratified flow. The roughness length is set to 0.014m and the Coriolis force is considered in the simulation.

Table 1: The physical parameters for some surface cover classes as used in MITRAS.

Class	A [-]	z_0 [m]	K [m^2.s^{-1}]	ν [w.m^{-1}.K^{-1}]	α_q [-]	W_k [m]
water	0.10	0.00015	1.5×10^{-7}	0.58	0.98	100.0
asphalt	0.09	0.0003	2.3×10^{-6}	1.35	0.5	0.0015
sand	0.10	0.03	2.4×10^{-7}	0.30	0.90	0.0677
cropland	0.20	0.04	5.2×10^{-6}	1.33	0.4	0.6
bushes	0.20	0.10	5.2×10^{-6}	1.33	0.15	0.06